Hindawi
Cellular Microbiology
Volume 2022, Article ID 3130361, 12 pages
https://doi.org/10.1155/2022/3130361

Research Article

A Live Cell Imaging Microfluidic Model for Studying Extravasation of Bloodborne Bacterial Pathogens

Michele d. Bergevin,[1,2,3] **Anna E. Boczula**,[3] **Laura-lee Caruso**,[1,2] **Henrik Persson**,[1,2] **Craig A. Simmons**,[1,2,3] **and Tara J. Moriarty**[3,4]

[1]*Department of Mechanical and Industrial Engineering, and Institute Biomedical Engineering, University of Toronto, 5 King's College Road, Toronto, ON, Canada M5S 3G8*
[2]*Translational Biology and Engineering Program, Ted Rogers Centre for Heart Research, 661 University Avenue, 14th Floor, Toronto, ON, Canada M5G 1M1*
[3]*Faculty of Dentistry, University of Toronto, 124 Edward Street, Toronto, ON, Canada M5G 1G6*
[4]*Faculty of Medicine, Department of Laboratory Medicine and Pathobiology, University of Toronto, Canada*

Correspondence should be addressed to Craig A. Simmons; c.simmons@utoronto.ca
and Tara J. Moriarty; tara.moriarty@utoronto.ca

Received 9 May 2022; Accepted 12 August 2022; Published 14 September 2022

Academic Editor: Barbara Kahl

Bacteria that migrate (extravasate) out of the bloodstream during vascular dissemination can cause secondary infections in many tissues and organs, including the brain, heart, liver, joints, and bone with clinically serious and sometimes fatal outcomes. The mechanisms by which bacteria extravasate through endothelial barriers in the face of blood flow-induced shear stress are poorly understood, in part because individual bacteria are rarely observed traversing endothelia *in vivo*, and *in vitro* model systems inadequately mimic the vascular environment. To enable the study of bacterial extravasation mechanisms, we developed a transmembrane microfluidics device mimicking human blood vessels. Fast, quantitative, three-dimensional live cell imaging in this system permitted single-cell resolution measurement of the Lyme disease bacterium *Borrelia burgdorferi* transmigrating through monolayers of primary human endothelial cells under physiological shear stress. This cost-effective, flexible method was 10,000 times more sensitive than conventional plate reader-based methods for measuring transendothelial migration. Validation studies confirmed that *B. burgdorferi* transmigrate actively and strikingly do so at similar rates under static and physiological flow conditions. This method has significant potential for future studies of *B. burgdorferi* extravasation mechanisms, as well as the transendothelial migration mechanisms of other disseminating bloodborne pathogens.

1. Introduction

Systemic dissemination of pathogens via the cardiovascular system is associated with most mortality due to bacterial infection. Many disseminating bacteria can interact stably with vascular surfaces, even in the face of blood flow-induced shear stress, and migrate out of vessels to extravascular tissues, an invasive process referred to as extravasation or transendothelial migration [1–3]. Extravasation can establish secondary sites of infection in critical organs such as brain, heart, and liver, as well as many other tissues including bone and joints [2].

Fluid shear stress is one of the most important barriers to transendothelial migration of bacteria in the cardiovascular system [1, 4]. Studying bacterial extravasation in the presence of shear stress is challenging because transmigration events are infrequent, making it difficult to investigate extravasation mechanisms in a direct, quantitatively robust fashion. As a result, most bacterial dissemination experiments were conducted under shear stress measure endpoint extravasation outcomes (e.g., detection of bacteria or bacterial components in tissues outside blood vessels). However, endpoint studies can be confounded by many factors, including the ability of bacteria to survive extravascular

immune responses [5, 6]. To date, the only direct observation of bacterial extravasation under vascular shear stress conditions has been achieved by real-time intravital microscopy (IVM) in the vasculature of live mice, and the only bacterial pathogen for which this process has been observed is *Borrelia burgdorferi*, the causative agent of Lyme disease [7–10].

B. burgdorferi is a highly motile bacterium with a flat sine wave morphology that can invade many organs and tissues [11]. *B. burgdorferi* extravasation in postcapillary venules and sinusoids of skin, joints, and liver can be very fast (<150 ms to penetrate endothelial lining of skin vessels, ~10 min to fully escape) [7–10], and studying this process in the highly dynamic environment of the vasculature requires high-speed microscopy approaches. However, IVM is time-, labor-, and cost-intensive. Since *B. burgdorferi* extravasation is a rare event, and filtering organs include the liver clear bacteria from the bloodstream [8], visualizing transmigration also requires intravenous injection of large numbers of microbes [10]. Although mice tolerate high *B. burgdorferi* densities in blood, injection of similar numbers of many other bacteria would induce rapid, acute inflammatory responses that alter cardiovascular function and blood flow, resulting in death [12]. Furthermore, intravascular clearance of microbes can make it challenging to study extravasation independent of the confounding effects of immune clearance [13]. Therefore, gaining deeper insight into extravasation mechanisms for many bacterial pathogens, including *B. burgdorferi*, will likely require complementary *in vitro* methods for studying transendothelial migration under physiological shear stress conditions.

Microfluidic models of the vasculature offer a promising approach for overcoming some barriers impeding investigation of bacterial extravasation mechanisms. An advantage of microfluidic systems is that the channel dimensions and controlled flow rates guarantee low Reynolds number, viscous laminar flow with predictable wall shear stresses [14]. Leukocyte and circulating cancer cell transendothelial migration have been studied in self-assembled 3D microvascular endothelial networks [15–18] or in side-by-side microchannels [19–24], in which cells migrate from one channel across a vertical endothelial monolayer into a second channel containing a hydrogel. Although microvascular networks mimic many aspects of the *in vivo* vasculature, their geometric complexity prevents precise control over shear stress and hinders imaging at the spatiotemporal resolution necessary for real-time visualization of bacterial transmigration. This is a particularly important problem for *B. burgdorferi*, since changes in shear stress affect the ability of these bacteria to interact stably with endothelia [25–28], and because their rapid movement and extravasation necessitates the use of real-time imaging. Side-by-side platforms address many of these limitations because of their planar geometry but hinder real-time evaluation of endothelial monolayer confluence and disrupt endothelial barrier integrity due to posts required for hydrogel retention within the central channel.

An alternative microfluidic configuration consists of two overlapping input and collecting microchannels that sandwich an optically transparent, porous Transwell membrane (Figure 1(a)). An endothelial monolayer is cultivated on the membrane in the input channel, and medium containing circulating cells (e.g., leukocytes or cancer cells) is perfused over the monolayer at precisely controlled flow rates that produce uniform shear stress at the apical surface of endothelial cells located at a central position equidistant from input channel walls and fluid inlets and outlets. The collection channel is bounded by a nonoptically transparent glass slide, permitting visualization of circulating cells that have successfully transmigrated through the endothelium. To date, this device design has been used to study transendothelial migration of cancer cells [29] and leukocytes [30, 31], which are relatively large and slow-moving, and tend to associate with the endothelium after extravasation.

However, this design is not compatible with high spatial and temporal resolution confocal imaging due to the thickness and optical properties of the glass slide and as such is limited to endpoint visualization techniques that require staining and visualization of endothelial monolayers and associated cells at experimental endpoints (i.e., not live). This poses a problem for studying extravasating bacteria, which are typically much smaller than leukocytes or tumor cells and thus more challenging to visualize under low spatial resolution conditions. Furthermore, *B. burgdorferi* is fast-moving, can swim rapidly in liquid filled input and collection channels, can penetrate endothelial monolayers under flow in <150 ms, and extravasates through these monolayers in less than 2 min [10]. Therefore, accurate extravasation measurements for most bacteria under flow, especially *B. burgdorferi*, require a capacity for high spatial resolution live cell imaging over the entire depth of collection channels.

The objectives of this study were twofold: to establish a physiologically relevant microfluidic model and sensitive real-time confocal image acquisition and analysis methods for accurately measuring extravasation of motile bacteria. These goals were achieved by adapting real-time, long working range IVM imaging techniques for visualizing and quantifying *B. burgdorferi* transendothelial migration in optically transparent, confocal microscopy-compatible transmembrane microfluidic devices. This system will be useful for studying extravasation mechanisms of *B. burgdorferi* and other bacterial pathogens under physiologically relevant shear stress conditions.

2. Methods

2.1. Transmembrane Device Design and Fabrication. As previously described [31, 32], device microchannels (input channel: 2.5 cm × 2 mm × ~ 200 μm and overlapping region of collection channel: 2 cm × 2 mm × 500 μm, length × width × height) were fabricated from polydimethylsiloxane (PDMS, 10 : 1) (Sylgard 184, Dow Corning, Midland, MI, USA) using standard soft lithography. Input and collection microchannels were fabricated using molded SU-8 (SU-8 50, Newton, MA USA) and aluminum masters, respectively. After overnight curing at 65-70°C, a biopsy punch was used to punch holes for inlet and outlet tubing and the slabs were trimmed and cleaned. The microchannel slabs were then bonded to a track-etched, transparent polyethylene

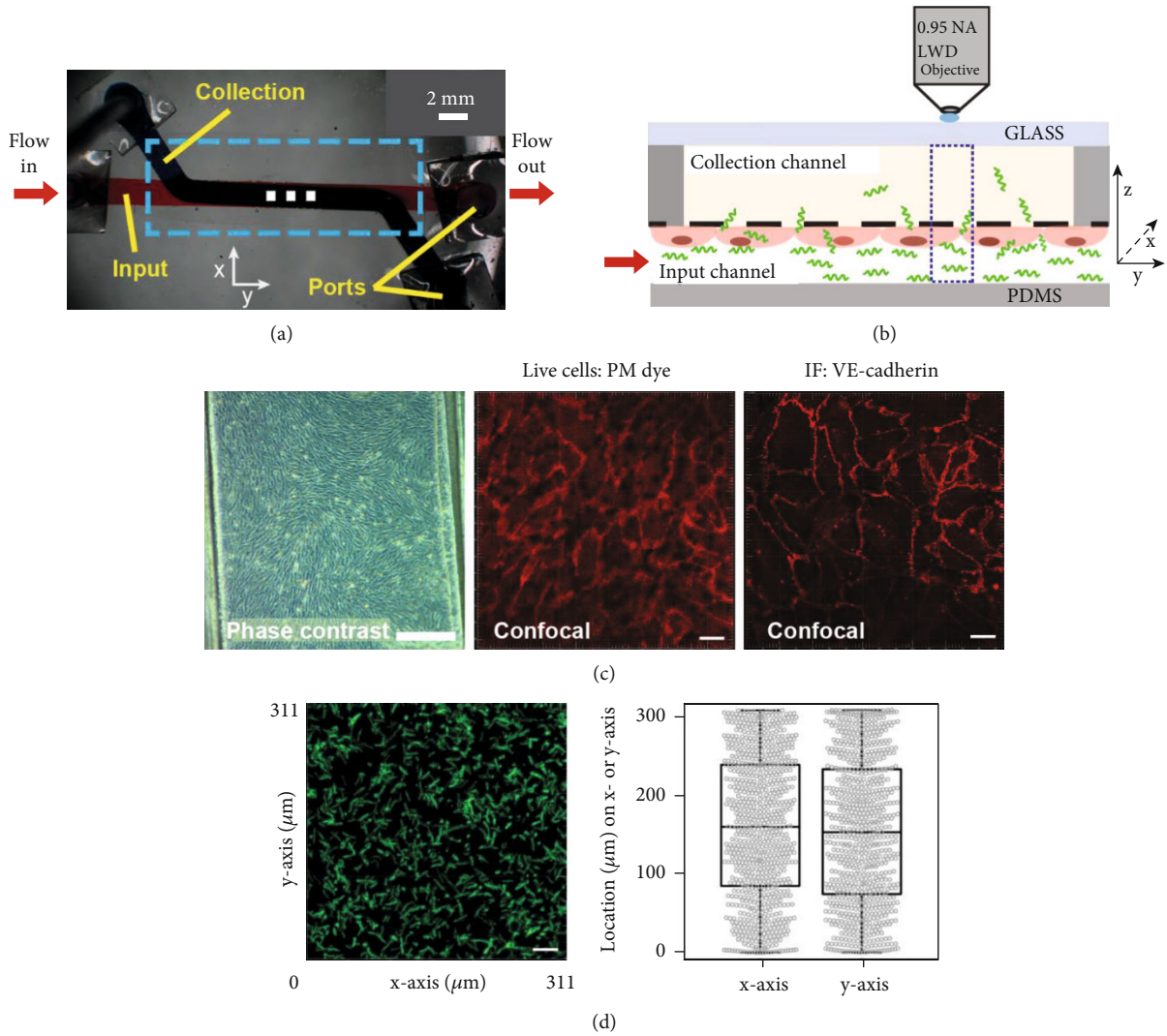

FIGURE 1: *In vitro* model to study endothelial transmigration of bacteria under physiological shear stress. (a) Microfluidic device, top view: PDMS input and collection channels sandwiching a porous, transparent membrane (blue box) coated with endothelia grown to 2 days postconfluence. White squares: imaging sites. (b) Cross-sectional schematic showing GFP-expressing B. burgdorferi (green) migrating from input to collection channels through endothelial monolayer stained with nontoxic live cell imaging plasma membrane dye (orange) and membrane (dashed black line). Red arrow: flow direction. At each imaging site, 3D *z*-series encompassing the full depth of input (~200 μm) and collection (~600 μm) channels were acquired at ~7 fps (~26 fps in *xy*) in 2 channels simultaneously, using a resonant scanning confocal microscope equipped with a high numerical aperture (NA) long working-distance (LWD) water-immersion objective. (c) Postconfluent endothelial monolayers in devices visualized by phase contrast microscopy (left: before experiments), resonant scanning confocal microscopy of live cells stained with plasma membrane dye (PM; middle), and immunofluorescence (IF) staining for endothelial junction protein VE-cadherin in fixed cells (right). Scale bars: 500 μm (phase contrast), 30 μm (PM, IF). (d) Representative 2-dimensional maximum intensity projection image (MIP) (left) and corresponding *xy* positions of bacteria (right: 25-75% interval boxplots) in the input channel from a 3D dataset captured under static conditions. *z*-series were captured before experiments to measure input channel depth and calculate flow rates required to achieve shear stress of 1 dyn/cm^2 at the endothelial surface and confirm uniform distribution of bacteria.

terephthalate (PET) membrane with 3 μm diameter pores obtained from Transwell chambers (Falcon, Corning/VWR International, Mississauga, ON, Canada) using PDMS : toluene mortar (5 : 4). The mortar was vortexed for 5 min in a glass vial and was spin coated (65 s at 1500 rpm) onto a clean glass slide (50 mm × 75 mm). The microchannel slabs were then placed on the mortar-coated glass slide for 1 min before assembly with the PET membrane. Devices were dried under weight ~2 kg at room temperature (RT°C) for 3 d and then bonded to No. 1 cover glass (24 mm × 60 mm; ThermoFisher Scientific, Ottawa, ON, Canada) after treatment of both PDMS and glass slide with an air plasma for 1 min (PE-100 Plasma System, Plasma Etch Inc., Carson City, NV, USA). Finally, tubing (PE-190, i.d. 1.19 mm, and o.d. 1.7 mm; Intramedic Clay Adams/Becon Dickinson, Mississauga, ON, Canada) was inserted into the punched channel ports and was anchored with plasma-treated PDMS adaptors followed by application of viscous, semicured PDMS that was allowed to cure at RT°C for an additional 3 days.

2.2. Cultivation of Endothelial Cells and Preparation for Imaging. Before seeding with endothelial cells (ECs), device channels were ethanol-sterilized and coated with 160 μg/ml bovine plasma fibronectin (bFn; Sigma-Aldrich Canada, Oakville, ON) for 2 h as previously described [31], followed by incubation at 37°C/5% CO_2 for 1 h. Early passage (maximum 4 passages) primary human umbilical vein endothelial cells pooled from multiple donors (HUVEC; Clonetics/Lonza, Mississauga, ON, Canada) cultivated as previously described [25] were resuspended to 2×10^6 cells/ml in cultivation medium and injected into input channels to achieve seeding densities of $\sim 4 \times 10^4$ cells/cm^2. Medium was replaced at 8 h and every 12 h thereafter until 2 d after cells reached confluence (3-4 d total). Immediately before imaging, endothelia were labeled with CellMask Deep Red (649/666 nm) plasma membrane live cell imaging dye (ThermoFisher) as previously described [25]; both channels were flushed with 37°C Hanks buffered saline (HBSS; ThermoFisher) containing 10% heat-inactivated fetal bovine serum (FBS; Sigma), and collection channel ports were plugged with vacuum grease. Transwell chambers incorporating the same membrane used in microfluidic devices were coated with bFn as described above, seeded with 1×10^6 HUVEC ($\sim 4 \times 10^4$ cells/cm^2) and cultivated to 2 d postconfluence with daily medium replacement (3 d total). Endothelia for Transwell experiments were not fluorescently labeled.

2.3. Preparation of B. burgdorferi and Beads for Imaging. As described [25], GFP-expressing B31 ML23-derived *B. burgdorferi* infectious strain GCB966 and noninfectious strain B31-A strain GCB706 [33–35] were cultivated, prepared for imaging, and resuspended to 4×10^7/ml in 37°C HBSS/10% FBS. GCB966 carries all plasmids known to encode *B. burgdorferi* adhesins, in addition to a plasmid lp25 gene encoding an intracellular nicotinamidase essential for infectivity but not adhesion [35–38]. The expression of all ~30 known and predicted adhesins has not been systematically profiled for GCB966, although the strain is infectious and presumably encodes many adhesins essential for infectivity. GCB706 does not genetically encode many *B. burgdorferi* adhesins [34]. Bacteria were counted in Petroff-Hausser chambers (Hausser Scientific 3900, ThermoFisher). For experiments involving microspheres, 2% w/v 0.22 μm 580/605 nm fluorescent carboxylate-modified microspheres (ThermoFisher) were vortexed 1 min, diluted to 4.5×10^8/ml in 37°C HBSS/10% FBS, vortexed 1-2 min, and mixed 3-5 times with a syringe and 18G needle before perfusion into devices.

2.4. Immunofluorescence Microscopy. HUVEC monolayers rinsed with 37°C magnesium- and calcium-containing phosphate-buffered saline ($PBS^{+/+}$; ThermoFisher) were fixed in ice-cold methanol for 15 min at -20°C, rinsed with magnesium- and calcium-free PBS ($PBS^{-/-}$; ThermoFisher), blocked 20 min 37°C in $PBS^{-/-}$ containing 3% w/v bovine serum albumin (BSA; Sigma), incubated 37°C 1 h with 3 μg/ml anti-VE-cadherin polyclonal antibody (Abcam, Toronto, ON, Canada, Cat. ab33168) in $PBS^{-/-}$/3% BSA, washed with 5 ml $PBS^{-/-}$, blocked 30 min RT°C with 10% heat-inactivated goat serum (Sigma) in $PBS^{-/-}$, then incubated 1 h RT°C in darkness with 0.025 μg/ml Alexa Fluor 488-conjugated goat anti-rabbit IgG antibody (ThermoFisher) in $PBS^{-/-}$/10% goat serum, washed with 5 ml $PBS^{-/-}$ and then 5 ml distilled water, mounted in Lerner Aqua-mount Mounting Medium (ThermoFisher), and stored 4°C in darkness until imaging. VE-cadherin immunofluorescence was visualized using a Leica SP8 confocal microscope (Leica Microsystems, Wetzlar, Germany) in conventional scanning mode, with 25 × 0.95 NA objective (1.5x zoom), 0.36 AU pinhole, HyD detector (100 gain), and ×10 frame averaging, at 488/499-742 nm (ex/em).

2.5. Static Transwell Experiments. 1 ml 37°C incubation medium (HBSS/10% FBS) containing 4×10^7 infectious bacteria (3 independent cultures) was added to HUVEC-coated transmembrane inserts ("input"), and 1 ml incubation medium alone was added to wells ("collection"), followed by 37°C/5% CO_2 incubation for duration of experiments. Every 30 min,100 μl samples from input and collection wells were transferred to a 96-well plate containing triplicate 2-fold serial dilutions of known numbers of GCB966 bacteria in incubation medium ("standards": range: 7.8×10^3-4×10^6 bacteria) and fluorescence intensities were measured using a Clariostar Monochromator Microplate Reader (BMG Labtech, Guelph, ON, Canada). After subtracting background fluorescence of incubation medium, numbers of bacteria in samples from input and collection wells were calculated from lines fit to the linear signal region for standards ($R^2 > 0.99$). Transmigration was calculated as the percentage of all bacteria (input and collection samples combined) in collection channels.

2.6. Microfluidic Transmembrane Device Experiments. All equipment except syringe pumps used for injection/perfusion (models: NE-1000 and NE-300; New Era Pump Systems, Farmingdale, NY, USA) were placed on the microscope air table, and ambient temperature was maintained at 29°C throughout experiments using a heat lamp and thermometer probe. Perfusion media was prewarmed prior to imaging, and the device, pump, and tubing were kept in a 37°C/5% CO_2 incubator between imaging sessions. Bacteria or beads were initially injected at 3.7 ml/h using a 20 ml syringe (Norm-Ject LS; ThermoFisher) connected to primed Tygon tubing (formulation 2375, i.d. 1.59 mm, and o.d. 3.18 mm; VWR). For static experiments, input channel ports were sealed after injection with vacuum grease. 3D datasets (z-series) encompassing the full depth of input and collection channels were immediately acquired at 3 non-overlapping positions (technical replicates) at the midpoint of input channels ($t = 0$ h) to measure input channel height. For the channel dimensions and shear stresses used here, flow is laminar (low Reynolds number viscous flow) with steady, predictable fluid streamlines that ensure uniform wall shear stresses in the central region of the channels [39]. As such, flow rates, Q (cm^3/s), required to achieve uniform wall shear stress $\tau_W = 1$ dyn/cm^2, at endothelial surfaces at the centre of channels were calculated from the channel width, $W = 2$ mm, and average input channel

height, H (μm), calculated from triplicate measurements, as described [39]:

$$Q = \tau_W \frac{(WH^2)}{2\mu}\left(\frac{m}{m+1}\right)\left(\frac{1}{n+1}\right), \quad (1)$$

where $m = 1.7 + 0.5(H/W)^{-1.4}$, $n = 2$, and viscosity, $\mu = 8.705 \times 10^{-3}$ dyn s/cm^2.

z-series encompassing the full depth of devices were acquired at 3 positions/timepoint over 4 h, at a central location equidistant from input channel walls, inlets, and outlets; then, triplicate z-series were captured under static conditions to count total bacteria in input and collection channels ($t_{endpoint}$). z-series with a depth of ~800 μm were acquired simultaneously in green (bacteria: 500-520 nm), orange (beads: 572-620 nm), and dark red (endothelia: 650-770 nm) channels (488, 561, and 633 nm lasers, respectively) in 512×512 pixel bidirectional resonant mode (gain 100, pinhole size 1.0 AU), using a Leica upright SP8 tandem scanner spectral confocal microscope equipped with HyD detectors, a 25×0.95 NA long working range water-immersion objective, and Leica acquisition software (LAS). Pixel and voxel dimensions were, respectively, $(0.607\,\mu m)^2$ and ~0.73 μm^3 for bacteria (1.5x zoom, 1.98 μm z-step size), and $(0.182\,\mu m)^2$ and ~0.03 μm^3 for beads (5x zoom, 0.99 μm z-step size). Image acquisition frame rates in xy were ~26 fps, but in z were ~7 fps due to time required for axial repositioning. Total z-series acquisition times for bacteria and beads were ~1 and 2 min, respectively.

2.7. Automated Object Quantification in z-Series. Bacteria and beads were counted in input and collection channels at $t = 0$ and $t_{endpoint}$ and in collection channels only at intervening timepoints, using the IMARIS software v.8.3.1 (Bitplane AG, Zurich, Switzerland) surface volume (grain size = 0.7 μm, min intensity = 40, and min volume = 10 μm^3) and spot (xy = 0.65 μm^2 and min intensity = 53) tools, respectively. Minimum intensity values for object counting were determined by measuring average background intensity in devices before injection of bacteria and beads. Images used for quantification were not subjected to postprocessing. Mean fold differences in object numbers measured by automated quantification compared to known numbers of input bacteria and beads were, respectively, 1.12 ± 0.22 and 1.11 ± 0.42 (SD). Objects were assigned to the collection channel if their centroid position lay below the z-plane marking the bottom of the endothelial monolayer, defined using the ortho slicer tool. Objects with centroids above this plane were assigned to the input channel. Transmigration was calculated as the number of objects in the collection channel expressed as a percentage of total objects counted in input and collection channels at $t_{endpoint}$. Best fit transmigration rate curves were obtained by linear regression (timepoints 0-4 h and 1-2.5 h for static and flow experiments, respectively).

2.8. Statistical Analysis. Statistical analysis and linear regression curve-fitting were performed in GraphPad Prism v.7.0 (GraphPad Software, La Jolla, CA, USA) using tests indicated in figure legends.

3. Results

3.1. Transmembrane Microfluidic System for Studying Bacterial Transendothelial Migration. To directly observe bacterial extravasation under physiologically relevant conditions, we built microfluidic devices in which a porous, optically transparent membrane was embedded between PDMS layers with input and collection microchannels mounted on a thin cover slip (Figure 1(a)). This design permitted confocal visualization of bacteria in both channels using a long working range objective (imaging depth > 1 mm; Figure 1(b)). Monolayers of primary human umbilical vein-derived endothelial cells (HUVECs) were cultivated under static conditions on membranes to 2 days postconfluence since maintaining endothelia in a postconfluent state increases *B. burgdorferi*-endothelial interactions under physiological shear stress [25] and monolayer barrier integrity [40], presumably due to maturation of endothelial intercellular junctions [41] and other surface structures and receptors encountered by bacteria. HUVECs were used in these proof-of-principle experiments to enable direct comparison to previous studies investigating B. burgdorferi-endothelial transmigration in Transwell devices under static conditions [42, 43], as well as *B. burgdorferi*-endothelial interaction mechanisms under postcapillary venule shear stress [25–28]. The HUVEC flow chamber model recapitulates all major molecular and biophysical properties of *B. burgdorferi* interactions with the walls of postcapillary venules in the skin of mice [25–27, 44]. Interaction of genetically diverse *Borrelia* strains with distinct tissue dissemination patterns with postconfluent HUVEC cultured under static conditions under postcapillary shear stress conditions also robustly predicts strain-specific dissemination to skin in intravenous (IV) perfusion infection models [44].

Since the diameters of *B. burgdorferi* and most bacteria are small (~0.3 and ~1 μm, respectively) [4, 45], monitoring endothelial barrier integrity in real time is critical for studying bacterial extravasation. Monolayer integrity during extravasation studies in microfluidic devices was monitored by prelabeling endothelia with a fluorescent, nontoxic live cell imaging plasma membrane dye that does not disrupt *B. burgdorferi*-endothelial interactions under shear stress [25] and that illuminated the periphery of endothelial cells with a staining pattern similar to that of intercellular junction component VE-cadherin (Figure 1(c)). This dye also distinguished between input and collection channels in confocal z-series. To ensure that input microchannels in devices used for transmigration experiments were patent and of uniform depth, we also confirmed that bacteria injected into devices were uniformly distributed in three dimensions throughout the input channel (Figure 1(d)). In the absence of endothelial cells, immediate, large-scale relocation of 0.2 μm control beads and bacteria to collecting channels from input channels was instantly observed under both static and flow conditions (Supp. Figure 1), indicating that the device membrane alone did not impede passage of beads or bacteria.

3.2. Single-Cell Quantification Method for Measuring Bacterial Transendothelial Migration. *B. burgdorferi* extravasation is a rare event [7, 10], and studying this process requires sensitive observation methods capable of detecting single bacteria. Additionally, *B. burgdorferi* swims through liquid medium at ~4 μm/s [46]. Therefore, accurately quantifying transmigration of this motile bacterium required the ability to perform simultaneous three-dimensional imaging of individual bacteria and endothelia at image acquisition rates faster than bacterial swim speed. Using a resonant scanner microscope equipped with multiple detectors, we simultaneously visualized *B. burgdorferi* expressing green fluorescent protein (GFP) and endothelia in three dimensions at ~26 and 7 frames/s (fps) in *xy* and *z* dimensions, respectively (~52 and 14 μm/s). To limit photobleaching of bacteria over time courses and achieve axial (*z*-axis) imaging speeds at least 3.5 times greater than bacterial swim speed, 3D datasets were captured with a *z*-step size (2 μm) that was larger than *B. burgdorferi* diameter. To compensate for reductions in spatial resolution required to achieve these imaging speeds, bacteria perfused over monolayers were diluted to a concentration at which they occupied ~0.01% of total sample volume. At this dilution, the probability that any three-dimensional pixel (voxel) contained more than one bacterium was negligible. This permitted counting of individual bacteria in input and collection channels using a volume-based object identification method (Figure 2(a), right panel).

To assess the sensitivity of imaging-based methods for enumerating *B. burgdorferi*, we compared bacterial counts in devices to numbers of bacteria measured by a fluorescent plate reader, the standard method used for quantifying *B. burgdorferi* transendothelial migration in conventional Transwell-based assays (Figure 2(b)) [42, 43, 47–49]. This comparison showed that imaging-based bacterial counting methods were >10,000 times more sensitive than plate reader-based methods. To determine the accuracy of imaging-based bacterial counting in microfluidic devices, we compared covariance within technical replicates for counts obtained by imaging devices to triplicate counts obtained in Petroff-Hausser chambers, which are used to measure *B. burgdorferi* concentrations in the samples flowed through microfluidic devices (Figure 2(c)). Measurement covariance did not differ significantly for these methods ($P > 0.5$). We also compared actual numbers of bacteria detected by imaging-based quantification to expected numbers of bacteria in each *z*-series, based on the volume of each *z*-series and the concentration of input bacteria measured by Petroff-Hausser chambers (Figure 2(d)). This showed that imaging-based counting identified all bacteria in devices, and that variation in actual vs. expected values was within the range of variation attributable to the error rate of Petroff-Hausser counting (Figure 2(d)). Therefore, we concluded that imaging-based methods for counting *B. burgdorferi* in microfluidic devices were accurate and substantially more sensitive than conventional plate reader-based detection methods.

3.3. Comparison of B. burgdorferi Transendothelial Migration in Microfluidic Devices and Transwells under Static Conditions. To determine if *B. burgdorferi* transendothelial migration was similar in microfluidic membrane devices and Transwells, we compared transmigration kinetics over a 4 h period under static conditions (Figure 3). We did not extend our studies beyond 4 h because visible holes began appearing in some monolayers in devices after this time point (data not shown). To monitor monolayer integrity in membrane devices over the full duration of experiments, we also measured nonspecific penetration of endothelial barriers by fluorescent beads with a diameter (0.2 μm) smaller than the thickness of *B. burgdorferi*. Small numbers of bacteria and beads were observed near the membrane in collection channels immediately after injection (Figure 3(a): $t = 0$ h), possibly because higher pressure in the input channel than in the collection channel during injection initially forced some bacteria and beads through small gaps between the membrane and walls of the devices. Although bead numbers in collection channels appeared to increase somewhat over time, values at 0 and all subsequent time points postinjection did not differ significantly ($P > .22$). This implied that although there was some nonspecific transport of beads into collection channels immediately following injection, monolayers remained largely impermeable and intact under static conditions for 4 h after injection.

The transmigration rate for bacteria was 3.9-fold greater than that of beads under static conditions in microfluidic devices ($3.80 \pm 0.45\%$ per h vs. $0.97 \pm 0.10\%$ per h, respectively; $P < .05$), with significant differences in the fractions of transmigrated bacteria vs. beads at 1.5 h and 4 h postinjection ($P < .05$) (Figure 3(b)). Since our quantification methods counted intact bacteria that had passed through monolayers to reach collection channels (i.e., not bacteria that were simply associated with monolayers), this implied that bacteria actively migrated through monolayers. Rates of bacterial transmigration in microfluidic devices and Transwells did not differ significantly ($3.80 \pm 0.45\%$ per h vs. $3.01 \pm 1.07\%$ per h, respectively; $P = .57$), indicating that these systems were functionally similar with respect to bacterial transmigration. Importantly, transmigration rates for Transwells were also similar to previously observed *B. burgdorferi* transendothelial migration rates for HUVEC monolayers in Transwells (2.4% per h) [42, 43]. Therefore, *B. burgdorferi* transendothelial migration in microfluidic and Transwell devices was comparable under static conditions.

3.4. Effects of Physiological Shear Stress on B. burgdorferi Transendothelial Migration. Finally, to determine how physiological shear stress affected transendothelial migration of *B. burgdorferi*, we measured transmigration rates for bacteria and control beads perfused over endothelial monolayers at flow rates that generated a shear stress of 1 dyn/cm^2 at the monolayer surface (Figure 4). This shear stress is typical in the postcapillary venules where *B. burgdorferi* extravasates *in vivo* [7, 10] and is also the shear stress at which *B. burgdorferi* interactions with endothelial monolayers in flow chambers are most abundant [25, 27]. In addition to the infectious *B. burgdorferi* strain used in device development experiments (Figures 1–3), we also used a noninfectious but motile adhesion-attenuated control *B. burgdorferi* strain that does not express many adhesins and is significantly impaired in the ability to interact with HUVEC in flow

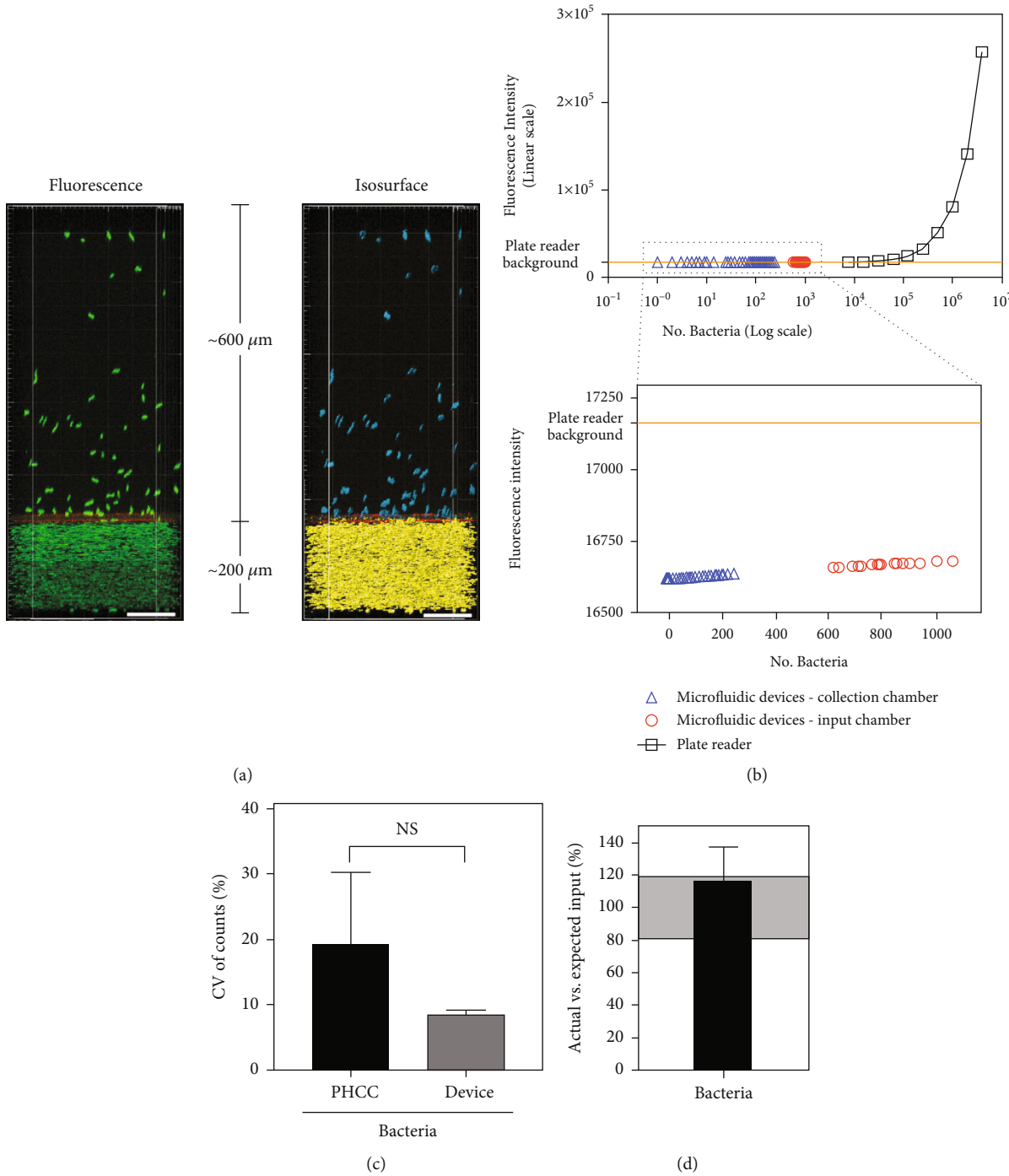

FIGURE 2: Focal depth, sensitivity, and accuracy of imaging-based bacterial quantification in microfluidic devices. (a) Sample 2-dimensional maximum intensity projection image of *z*-series showing *B. burgdorferi* transmigration through endothelia (red) after 1.5 h of flow (left),\ and isosurface-rendered bacteria identified in the input (yellow) and collection (blue) channels of the same *z*-series by volumetric object counting. Scale bar: 100 μm. (b) Sensitivity comparison of imaging- and plate reader-based bacterial quantification methods. Orange line: background fluorescence intensity of perfusion buffer in plate reader. Inset: magnified view of region in upper graph indicated by dashed box. Fluorescence intensity values for bacteria counted in 3D imaging datasets were extrapolated from standard intensity vs. bacterial number curves from plate reader samples. (c, d) Precision and accuracy of bacterial counting by volumetric object identification in *z*-series. In (c), the coefficient of variation (CV) for triplicate *z*-series acquired at multiple locations in each microfluidic device was compared to CV for bacterial counts in Petroff-Hausser counting chambers (PHCC) used to measure input numbers of bacteria. NS: not significant ($P > .05$; two-tailed *t* -test). $N = 3$ independent microfluidic devices, 3 independent bacterial cultures (PHCC). (d) Numbers of bacteria counted by volumetric object identification in input channels under no-flow conditions before experiments ("actual") compared to numbers of bacteria expected within each *z*-stack based on input numbers calculated from PHCC measurements. Gray shading: CV of PHCC counts (i.e., expected input measurement variation). All figure summary values = mean ± SD. In (b), most error bars are too small to be visible.

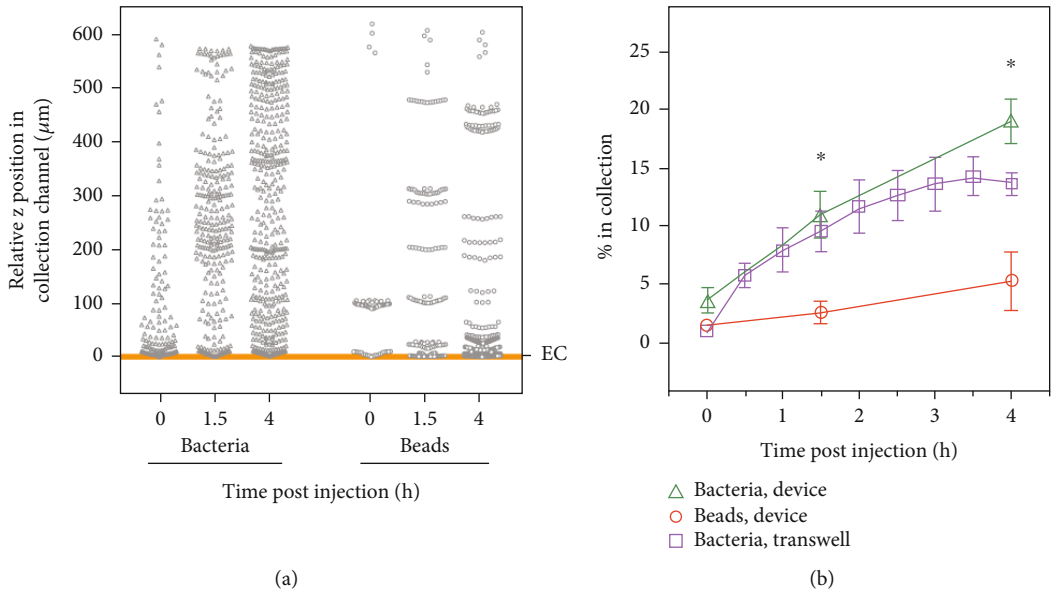

FIGURE 3: Validation of microfluidic *B. burgdorferi* transmigration system under static conditions. (a) Numbers of infectious bacteria and 0.2 μm beads at indicated z-positions and timepoints in collection channels of 3 independent microfluidic devices/group (composite numbers for 3 devices). Orange line: endothelial cell (EC) monolayer position. (b) Mean ± SEM percentages of total bacteria and beads per device located in collection channels at indicated timepoints, calculated as a percentage of total numbers measured in input and collection channels at $t = 4$ h by imaging-based counting method. Transwell: percentage of total bacteria counted by plate reader in collection chambers of conventional Transwell devices. $N = 3$ independent bacterial and endothelial cultures per group. Statistics: repeated measures 2-way ANOVA and Holm-Sidak posttest. $^*P < .05$ (beads vs. bacteria within timepoint in both Transwell and microfluidic devices).

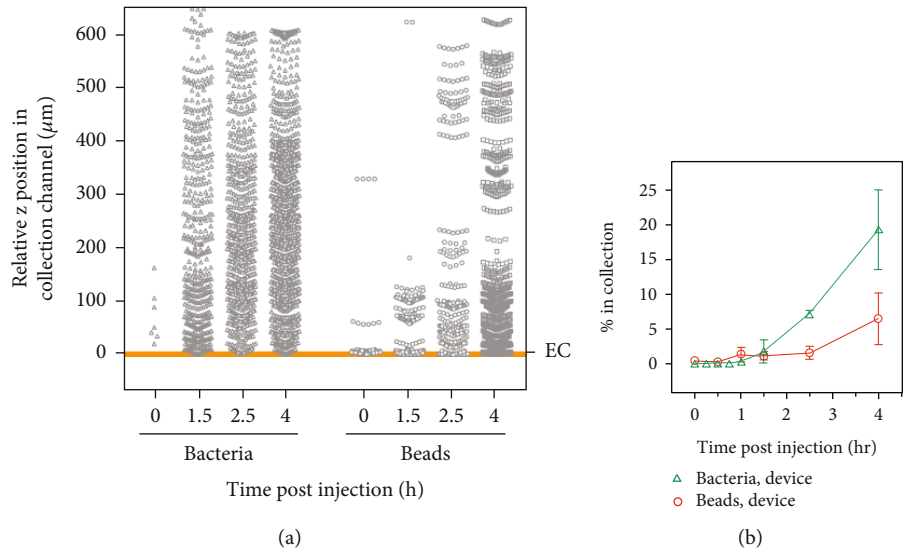

FIGURE 4: *B. burgdorferi* transmigration through endothelial monolayers in microfluidic devices at physiological shear stress (1 dyn/cm^2). (a) Composite numbers of infectious bacteria and beads at indicated z-positions and timepoints in collection channels of 3 independent devices/group. Orange line: endothelial cell (EC) monolayer. (b) Mean ± SEM percentage of total bacteria (infectious and noninfectious strains) and beads in collection channels at indicated timepoints, expressed relative to total counts in input and collection channels after $t = 2.5$ h of perfusion. $N = 3$ independent bacterial, endothelial cultures, and devices per group. Statistics: repeated measures 2-way ANOVA and Holm-Sidak posttest. $^*P < .05$ for infectious compared to noninfectious bacteria and beads at each timepoint.

chambers or with dermal postcapillary venules of mice [25, 26, 34]. Perfusion was performed for 2.5 h, since holes began appearing in monolayers in some devices at 4 h (data not shown). Transendothelial migration of infectious *B. burgdorferi* began later under shear stress (Figure 4) than static conditions (Figure 3). However, from 1 h postinjection, transmigration rates under shear stress were 3.5-fold greater for infectious bacteria than beads (4.94 ± 0.84% per hr vs. 1.42 ± 0.35% per hr, respectively; $P < .05$) and were comparable to transmigration rates under static conditions

($P = 0.38$). Accumulation of noninfectious, adhesion-attenuated bacteria in the collection channel 2.5 hours after injection was significantly reduced compared to the infectious strain ($P < .0001$) and did not differ from accumulation of beads ($P > .36$) (Figure 4(b)). Therefore, despite delayed onset of transmigration of infectious bacteria under flow, once this process started, it appeared to be as efficient as transmigration under static conditions.

4. Discussion

To address the limitations of current bacterial extravasation models, we engineered an imaging-compatible transmembrane microfluidic device paired with multichannel long working range IVM visualization methods to achieve fast, sensitive, quantitative analysis of *B. burgdorferi* transendothelial migration under physiological shear stress. Consistent with previous studies implicating *B. burgdorferi* motility in transendothelial migration under static conditions *in vitro* and in postcapillary venules *in vivo* [8, 10, 43, 50], we found that infectious *B. burgdorferi* actively transmigrates compared to control beads, with similar kinetics in microfluidic devices and Transwells under static conditions. Transmigration also depended on the ability of bacteria to interact with endothelial cells under flow, since a fully motile, adhesion-attenuated noninfectious control strain did not traverse monolayers any more than control beads. *B. burgdorferi* extravasation rates in our Transwell experiments and in the microfluidic system were also similar to previously reported *B. burgdorferi* transmigration rates through HUVEC in Transwells [42, 43]. These transmigration rates were at least two orders of magnitude greater than *B. burgdorferi* transmigration rates reported for monolayers of primary human brain endothelial cells or brain endothelial-derived cell lines in Transwells, consistent with the enhanced barrier function of brain endothelia [47, 48]. Therefore, the transmembrane microfluidic system provides a biologically relevant model for studying *B. burgdorferi* extravasation under vascular shear stress conditions. Furthermore, the accurate single-cell quantification capabilities of this system increased extravasation detection sensitivity 10,000-fold compared to conventional plate reader-based methods for measuring extravasation in static Transwells. This greatly improves the ability to study mechanisms supporting rare bacterial transendothelial migration events, under controlled *in vitro* conditions where confounding variables such as immune clearance are absent and where molecular components of the extravasation process can be more readily dissected.

Our study showed that under shear stress conditions mimicking the physiological microenvironment in blood vessels, *B. burgdorferi* transmigration onset was delayed, but extravasation kinetics after onset were similar under static and flow conditions, possibly because bacteria settled onto endothelia under static conditions, increasing the probability of endothelial contact and early transmigration. *B. burgdorferi* transendothelial migration under flow may also require changes in the expression, activation, and/or localization of endothelial cell surface adhesion molecules or proteases and adherens junction components regulating endothelial permeability. This hypothesis is consistent with previous reports that endothelia exposed to live *B. burgdorferi* and isolated surface lipoproteins promote leukocyte transmigration [51, 52] and induce expression and activation of endothelial surface receptors and proteases regulating leukocyte recruitment [48, 52–55]. Although *B. burgdorferi* extravasation occurs immediately upon intravenous inoculation in dermal postcapillary venules of mice [10], extravasated *B. burgdorferi* is not observed until 24 h after inoculation in joints [7], implying that bacterial transmigration may require active participation of endothelial cells in the vascular beds of some tissues. Since exposing endothelial monolayers to shear stress induces rapid changes in the composition, organization, and cytoskeletal anchoring of permeability-regulating endothelial adherens junction proteins [56–59], delayed *B. burgdorferi* transmigration under flow might also reflect shear stress-dependent changes in endothelial barrier function, particularly if generalized endothelial inflammatory changes alter blood flow properties. Although it has not yet been determined if shear stress affects *B. burgdorferi* protein expression and localization, it is also possible that such changes could contribute to delayed bacterial transendothelial migration under flow. Investigation of the potential contributions of endothelial activation and junction rearrangement to transmigration mechanisms using a microfluidic transmembrane model will require the ability to cocultivate primary endothelial cells and *B. burgdorferi* for periods longer than 4 hours, which we have unfortunately not yet been able to technically achieve. In addition, leukocyte molecular transmigration mechanisms differ in distinct vascular beds, and genetically diverse *Borrelia* strains also exhibit distinct interaction affinities for endothelia from the vascular beds of different tissues under physiological shear stress [44]. Thus, factors specific to endothelia in different tissues likely also influence *B. burgdorferi* transendothelial migration kinetics and mechanisms. Finally, although professional phagocytic cells such as Kupffer cells that filter blood likely remove the bulk of *B. burgdorferi* from the bloodstream [8], it is possible that endothelial cells themselves could contribute to clearance of bloodborne *Borrelia*, due to their ability to internalize/be invaded by these bacteria [35, 42, 50, 60, 61].

The flexible design, sensitivity, and precision of the high-speed imaging-based microfluidic transmembrane system reported here support its use as a model for studying extravasation mechanisms of multiple bloodborne pathogens. The cost-effectiveness and technical ease of this system compared to animal models may also facilitate development of therapeutic approaches for inhibiting bacterial dissemination via the bloodstream.

Data Availability

The data used to support the findings of this study are available from the corresponding author upon request.

Additional Points

Key Points. Fast 3D imaging in a blood vessel-mimicking microfluidic device enables measurement of bacterial extravasation at single-cell resolution.

Conflicts of Interest

The authors declare that the research was conducted in the absence of any commercial or financial relationships that could be construed as a potential conflict of interest.

Authors' Contributions

Conception and design were contributed by MB, CS, and TM. Methodology development was done by MB, LC, HP, CS, and TM. Data acquisition was carried out by MB and AB. Data analysis and interpretation were done by MB, CS, and TM. Manuscript writing and revision were performed by MB, LC, HP, AB, CS, and TM. Study supervision and funding were contributed by CS and TM.

Acknowledgments

This study was supported by the following operating funds: Collaborative Health Research Project operating grant to TM and CS from the Natural Science and Engineering Research Council (NSERC) of Canada and the Canadian Institutes of Health Research (CHRPJ 446650-13 and CPG-127788), NSERC operating grants to CS (RGPIN-2016-06026) and TM (RGPIN-2011-401938), and CIHR operating grants to TM (MOP-11959 and ICS-12398). Infrastructure was by the Canada Foundation for Innovation/Ontario Research Fund (CFI/ORF) to TM. Salary support was by the Graduate scholarships to MB from NSERC CREATE Program in Microfluidic Applications and Training in Cardiovascular Health (MATCH), Heart and Stroke/Richard Lewar Centre of Excellence in Cardiovascular Research, and Barbara and Frank Milligan, all at the University of Toronto. The authors gratefully acknowledge training, technical, and facility support from the University of Toronto Centre for Microfluidics Systems (Lindsey Fiddes), Sick Kids Hospital Imaging Facility (Michael Woodside, Paul Paroutis), Matrix Dynamics Group (Mariya Kovalyuk), laboratory of Boris Hinz, and Anil Bansal, Zahra Mirzaei, Aleks Chebotarev, Amy Zhao, and Nataliya Zlotnikov. We thank Simmons and Moriarty lab members for providing additional training and helpful discussion.

Supplementary Materials

Supplemental Figure 1: unimpeded passage of control beads and *B. burgdorferi* through microfluidic device membrane in the absence of endothelial cells. *(Supplementary Materials)*

References

[1] M. Coureuil, H. Lécuyer, S. Bourdoulous, and X. Nassif, "A journey into the brain: insight into how bacterial pathogens cross blood–brain barriers," *Nature Reviews Microbiology*, vol. 15, no. 3, pp. 149–159, 2017.

[2] E. Lemichez, M. Lecuit, X. Nassif, and S. Bourdoulous, "Breaking the wall: targeting of the endothelium by pathogenic bacteria," *Nature Reviews. Microbiology*, vol. 8, no. 2, pp. 93–104, 2010.

[3] A. Lubkin and V. J. Torres, "Bacteria and endothelial cells: a toxic relationship," *Current Opinion in Microbiology*, vol. 35, pp. 58–63, 2017.

[4] A. Persat, C. D. Nadell, M. K. Kim et al., "The mechanical world of bacteria," *Cell*, vol. 161, no. 5, pp. 988–997, 2015.

[5] D. Bumann, "Heterogeneous host-pathogen encounters: act locally, think globally," *Cell Host & Microbe*, vol. 17, no. 1, pp. 13–19, 2015.

[6] G. T. Crimmins and R. R. Isberg, "Analyzing microbial disease at high resolution: following the fate of the bacterium during infection," *Current Opinion in Microbiology*, vol. 15, no. 1, pp. 23–27, 2012.

[7] D. Kumar, L. C. Ristow, M. Shi et al., "Intravital imaging of vascular transmigration by the Lyme spirochete: requirement for the integrin binding residues of the B. burgdorferi P66 protein," *PLoS Pathogens*, vol. 11, no. 12, article e1005333, 2015.

[8] W.-Y. Lee, T. J. Moriarty, C. H. Y. Wong et al., "An intravascular immune response to Borrelia burgdorferi involves Kupffer cells and iNKT cells," *Nature Immunology*, vol. 11, no. 4, pp. 295–302, 2010.

[9] W.-Y. Lee, M.-J. Sanz, C. H. Y. Wong et al., "Invariant natural killer T cells act as an extravascular cytotoxic barrier for joint-invading Lyme Borrelia," *Proc Natl Acad Sci USA*, vol. 111, no. 38, pp. 13936–13941, 2014.

[10] T. J. Moriarty, M. U. Norman, P. Colarusso, T. Bankhead, P. Kubes, and G. Chaconas, "Real-time high resolution 3D imaging of the Lyme disease spirochete adhering to and escaping from the vasculature of a living host," *PLoS Pathogens*, vol. 4, no. 6, article e1000090, 2008.

[11] A. C. Steere, F. Strle, G. P. Wormser et al., "Lyme borreliosis," *Nature Reviews Disease Primers*, vol. 2, no. 1, article 16090, 2016.

[12] G. Ramachandran, "Gram-positive and gram-negative bacterial toxins in sepsis: a brief review," *Virulence*, vol. 5, no. 1, pp. 213–218, 2014.

[13] M. Harding and P. Kubes, "Innate immunity in the vasculature: interactions with pathogenic bacteria," *Current Opinion in Microbiology*, vol. 15, no. 1, pp. 85–91, 2012.

[14] E. W. Young and C. A. Simmons, "Macro- and microscale fluid flow systems for endothelial cell biology," *Lab on a Chip*, vol. 10, no. 2, pp. 143–160, 2010.

[15] M. Chen, J. Lamar, R. Li, R. Hynes, and R. Kamm, "Elucidation of the roles of tumor integrin β_1 in the extravasation stage of the metastasis cascade," *Cancer Research*, vol. 76, no. 9, pp. 2513–2524, 2016.

[16] M. Chen, J. Whisler, J. Jeon, and R. Kamm, "Mechanisms of tumor cell extravasation in an in vitro microvascular network platform," *Integrative Biology*, vol. 5, no. 10, pp. 1262–1271, 2013.

[17] J. Jeon, S. Bersini, M. Gilardi et al., "Human 3D vascularized organotypic microfluidic assays to study breast cancer cell extravasation," *Proceedings of the National Academy of Sciences*, vol. 112, no. 1, pp. 214–219, 2015.

[18] A. Wong and P. Searson, "Live-cell imaging of invasion and intravasation in an artificial microvessel platform," *Cancer Research*, vol. 74, no. 17, pp. 4937–4945, 2014.

[19] S. Bersini, J. Jeon, G. Dubini et al., "A microfluidic 3D in vitro model for specificity of breast cancer metastasis to bone," *Biomaterials*, vol. 35, no. 8, pp. 2454–2461, 2014.

[20] S. Han, J. J. Yan, Y. Shin et al., "A versatile assay for monitoring in vivo-like transendothelial migration of neutrophils," *Lab on a Chip*, vol. 12, no. 20, pp. 3861–3865, 2012.

[21] J. Jeon, I. Zervantonakis, S. Chung, R. Kamm, and J. Charest, "In vitro model of tumor cell extravasation," *PLoS One*, vol. 8, no. 2, article e56910, 2013.

[22] Y. Shin, S. Han, J. Jeon et al., "Microfluidic assay for simultaneous culture of multiple cell types on surfaces or within hydrogels," *Nature Protocols*, vol. 7, no. 7, pp. 1247–1259, 2012.

[23] I. Zervantonakis, S. Hughes-Alford, J. Charest, J. Condeelis, F. Gertler, and R. Kamm, "Three-dimensional microfluidic model for tumor cell intravasation and endothelial barrier function," *Proceedings of the National Academy of Sciences*, vol. 109, no. 34, pp. 13515–13520, 2012.

[24] Q. Zhang, T. Liu, and J. Qin, "A microfluidic-based device for study of transendothelial invasion of tumor aggregates in realtime," *Lab on a Chip*, vol. 12, no. 16, pp. 2837–2842, 2012.

[25] R. Ebady, A. F. Niddam, A. E. Boczula et al., "Biomechanics of Borrelia burgdorferi vascular interactions," *Cell Reports*, vol. 16, no. 10, pp. 2593–2604, 2016.

[26] W.-C. A. Kao, H. Pětrošová, R. Ebady et al., "Identification of Tp0751 (pallilysin) as a Treponema pallidum vascular adhesin by heterologous expression in the Lyme disease spirochete," *Scientific Reports*, vol. 7, no. 1, p. 1538, 2017.

[27] A. F. Niddam, R. Ebady, A. Bansal, A. Koehler, B. Hinz, and T. J. Moriarty, "Plasma fibronectin stabilizes Borrelia burgdorferi-endothelial interactions under vascular shear stress by a catch-bond mechanism," *Proc Natl Acad Sci USA*, vol. 114, no. 17, pp. E3490–E3498, 2017.

[28] J. Salo, A. Pietikäinen, M. Söderström et al., "Flow-tolerant adhesion of a bacterial pathogen to human endothelial cells through interaction with biglycan," *The Journal of Infectious Diseases*, vol. 213, no. 10, pp. 1623–1631, 2016.

[29] J. Song, S. Cavnar, A. Walker et al., "Microfluidic endothelium for studying the intravascular adhesion of metastatic breast cancer cells," *PLoS One*, vol. 4, no. 6, article e5756, 2009.

[30] D. Huh, B. Matthews, A. Mammoto, M. Montoya-Zavala, H. Hsin, and D. Ingber, "Reconstituting organ-level lung functions on a chip," *Science*, vol. 328, no. 5986, pp. 1662–1668, 2010.

[31] S. Srigunapalan, C. Lam, A. R. Wheeler, and C. A. Simmons, "A microfluidic membrane device to mimic critical components of the vascular microenvironment," *Biomicrofluidics*, vol. 5, no. 1, p. 013409, 2011.

[32] M. Chen, S. Srigunapalan, A. R. Wheeler, and C. A. Simmons, "A 3D microfluidic platform incorporating methacrylated gelatin hydrogels to study physiological cardiovascular cell-cell interactions," *Lab on a Chip*, vol. 13, no. 13, pp. 2591–2598, 2013.

[33] T. J. Moriarty, M. Shi, Y.-P. Lin et al., "Vascular binding of a pathogen under shear force through mechanistically distinct sequential interactions with host macromolecules," *Molecular Microbiology*, vol. 86, no. 5, pp. 1116–1131, 2012.

[34] M. U. Norman, T. J. Moriarty, A. R. Dresser, B. Millen, P. Kubes, and G. Chaconas, "Molecular mechanisms involved in vascular interactions of the Lyme disease pathogen in a living host," *PLoS Pathogens*, vol. 4, no. 10, article e1000169, 2008.

[35] J. Wu, E. H. Weening, J. B. Faske, M. Hook, and J. T. Skare, "Invasion of eukaryotic cells by Borrelia burgdorferi requires β_1 integrins and Src kinase activity," *Infection and Immunity*, vol. 79, no. 3, pp. 1338–1348, 2011.

[36] M. Labandeira-Rey and J. T. Skare, "Decreased infectivity in Borrelia burgdorferi strain B31 is associated with loss of linear plasmid 25 or 28-1," *Infection and Immunity*, vol. 69, no. 1, pp. 446–455, 2001.

[37] J. E. Purser, M. B. Lawrenz, M. J. Caimano, J. K. Howell, J. D. Radolf, and S. J. Norris, "A plasmid-encoded nicotinamidase (PncA) is essential for infectivity of Borrelia burgdorferi in a mammalian host," *Molecular Microbiology*, vol. 48, no. 3, pp. 753–764, 2003.

[38] J. Seshu, M. D. Esteve-Gassent, M. Labandeira-Rey et al., "Inactivation of the fibronectin-binding adhesin gene bbk32 significantly attenuates the infectivity potential of Borrelia burgdorferi," *Molecular Microbiology*, vol. 59, no. 5, pp. 1591–1601, 2006.

[39] E. W. Young, A. R. Wheeler, and C. A. Simmons, "Matrix-dependent adhesion of vascular and valvular endothelial cells in microfluidic channels," *Lab on a Chip*, vol. 7, no. 12, pp. 1759–1766, 2007.

[40] N. Douville, Y. Tung, R. Li, J. Wang, M. El-Sayed, and S. Takayama, "Fabrication of two-layered channel system with embedded electrodes to measure resistance across epithelial and endothelial barriers," *Analytical Chemistry*, vol. 82, no. 6, pp. 2505–2511, 2010.

[41] M. Lampugnani, M. Corada, L. Caveda et al., "The molecular organization of endothelial cell to cell junctions: differential association of plakoglobin, beta-catenin, and alpha-catenin with vascular endothelial cadherin (VE-cadherin)," *The Journal of Cell Biology*, vol. 129, no. 1, pp. 203–217, 1995.

[42] L. E. Comstock and D. D. Thomas, "Penetration of endothelial cell monolayers by Borrelia burgdorferi," *Infection and Immunity*, vol. 57, no. 5, pp. 1626–1628, 1989.

[43] A. Sadziene, D. D. Thomas, V. G. Bundoc, S. C. Holt, and A. G. Barbour, "A flagella-less mutant of Borrelia burgdorferi. Structural, molecular, and in vitro functional characterization," *The Journal of Clinical Investigation*, vol. 88, no. 1, pp. 82–92, 1991.

[44] A. E. Boczula, A. Ly, R. Ebady et al., "Vascular tropism models of blood-borne microbial dissemination," *bioRxiv*, vol. 5, no. 5, article 442761, 2021.

[45] N. W. Charon, A. Cockburn, C. Li et al., "The unique paradigm of spirochete motility and chemotaxis," *Annual Review of Microbiology*, vol. 66, no. 1, pp. 349–370, 2012.

[46] S. F. Goldstein, N. W. Charon, and J. A. Kreiling, "Borrelia burgdorferi swims with a planar waveform similar to that of eukaryotic flagella," *Proc Natl Acad Sci USA*, vol. 91, no. 8, pp. 3433–3437, 1994.

[47] D. J. Grab, E. Nyarko, O. V. Nikolskaia, Y. V. Kim, and J. S. Dumler, "Human brain microvascular endothelial cell traversal by Borrelia burgdorferi requires calcium signaling," *Clinical Microbiology and Infection*, vol. 15, no. 5, pp. 422–426, 2009.

[48] D. J. Grab, G. Perides, J. S. Dumler et al., "Borrelia burgdorferi, host-derived proteases, and the blood-brain barrier," *Infection and Immunity*, vol. 73, no. 2, pp. 1014–1022, 2005.

[49] A. Szczepanski, M. Furie, J. Benach, B. Lane, and H. Fleit, "Interaction between Borrelia burgdorferi and endothelium in vitro," *The Journal of Clinical Investigation*, vol. 85, no. 5, pp. 1637–1647, 1990.

[50] L. E. Comstock and D. D. Thomas, "Characterization of Borrelia burgdorferi invasion of cultured endothelial cells," *Microbial Pathogenesis*, vol. 10, no. 2, pp. 137–148, 1991.

[51] E. I. Gergel and M. B. Furie, "Activation of endothelium by Borrelia burgdorferi in vitro enhances transmigration of specific subsets of T lymphocytes," *Infection and Immunity*, vol. 69, no. 4, pp. 2190–2197, 2001.

[52] T. J. Sellati, M. J. Burns, M. A. Ficazzola, and M. B. Furie, "Borrelia burgdorferi upregulates expression of adhesion molecules on endothelial cells and promotes transendothelial migration of neutrophils in vitro," *Infection and Immunity*, vol. 63, no. 11, pp. 4439–4447, 1995.

[53] K. Ebnet, K. D. Brown, U. K. Siebenlist, M. M. Simon, and S. Shaw, "Borrelia burgdorferi activates nuclear factor-κB and is a potent inducer of chemokine and adhesion molecule gene expression in endothelial cells and fibroblasts," *Journal of Immunology*, vol. 158, pp. 3285–3292, 1997.

[54] T. J. Sellati, L. D. Abrescia, J. D. Radolf, and M. B. Furie, "Outer surface lipoproteins of Borrelia burgdorferi activate vascular endothelium in vitro," *Infection and Immunity*, vol. 64, no. 8, pp. 3180–3187, 1996.

[55] R. M. Wooten, V. R. Modur, T. M. McIntyre, and J. J. Weis, "Borrelia burgdorferi outer membrane protein a induces nuclear translocation of nuclear factor-κB and inflammatory activation in human endothelial cells," *Journal of Immunology*, vol. 157, pp. 4584–4590, 1996.

[56] M. Giannotta, M. Trani, and E. Dejana, "VE-cadherin and endothelial adherens junctions: active guardians of vascular integrity," *Developmental Cell*, vol. 26, no. 5, pp. 441–454, 2013.

[57] Y. A. Komarova, K. Kruse, D. Mehta, and A. B. Malik, "Protein interactions at endothelial junctions and signaling mechanisms regulating endothelial permeability," *Circulation Research*, vol. 120, no. 1, pp. 179–206, 2017.

[58] S. Noria, D. Cowman, A. Gotlieb, and B. Langille, "Transient and steady-state effects of shear stress on endothelial cell adherens junctions," *Circulation Research*, vol. 85, no. 6, pp. 504–514, 1999.

[59] J. M. Tarbell, S. I. Simon, and F.-R. E. Curry, "Mechanosensing at the vascular interface," *Annual Review of Biomedical Engineering*, vol. 16, no. 1, pp. 505–532, 2014.

[60] J. A. Hyde, "Borrelia burgdorferi keeps moving and carries on: a review of borrelial dissemination and invasion," *Frontiers in Immunology*, vol. 8, p. 114, 2017.

[61] Y. Ma, A. Sturrock, and J. J. Weis, "Intracellular localization of Borrelia burgdorferi within human endothelial cells," *Infection and Immunity*, vol. 59, no. 2, pp. 671–678, 1991.